Integrative Biology

PAPER

Cite this: *Integr. Biol.*, 2018, **10**, 194

Shear dependent red blood cell adhesion in microscale flow†

Erdem Kucukal,[a] Jane A. Little[bc] and Umut A. Gurkan *[ade]

Received 9th January 2018,
Accepted 8th March 2018

DOI: 10.1039/c8ib00004b

rsc.li/integrative-biology

Non-adherence and deformability are the key intrinsic biomechanical features of the red blood cell (RBC), which allow it to tightly squeeze and pass through even the narrowest of microcirculatory networks. Blockage of microcirculatory flow, also known as vaso-occlusion, is a consequence of abnormal cellular adhesion to the vascular endothelium. In sickle cell disease (SCD), an inherited anaemia, even though RBCs have been shown to be heterogeneous in adhesiveness and deformability, this has not been studied in the context of physiologically relevant dynamic shear gradients at the microscale. We developed a microfluidic system that simulates physiologically relevant shear gradients of microcirculatory blood flow at a constant single volumetric flow rate. Using this system, shear dependent adhesion of RBCs from 28 subjects with SCD and from 11 healthy subjects was investigated using vascular endothelial protein functionalized microchannels. We defined a new term, RBC Shear Gradient Microfluidic Adhesion (SiGMA) index to assess shear dependent RBC adhesion in a subject-specific manner. We have shown for the first time that shear dependent adhesion of RBCs is heterogeneous in a microfluidic flow model, which correlates clinically with inflammatory markers and iron overload in subjects with SCD. This study reveals the complex dynamic interactions between RBC-mediated microcirculatory occlusion and clinical outcomes in SCD. These interactions may also be relevant to other microcirculatory disorders and microvascular diseases.

Insight, innovation, integration

This paper reports on the shear dependent adhesion behavior of red blood cells (RBCs) using a physiologically relevant shear gradient microfluidic system. The uniqueness of the presented approach is the ability to observe adhesion phenomenon at single cell level within a shear gradient in clinical blood samples, rather than employing systems with discrete or constant shear values. In this study, shear dependent adhesion of RBCs in twenty-eight subjects with sickle cell disease and in eleven healthy individuals was assessed. A new, clinically relevant parameter has been introduced for the first time, RBC Shear Gradient Microfluidic Adhesion (SiGMA) index, which can be used to assess shear dependent RBC adhesion in a subject-specific manner. Results showed significant clinical associations between shear dependency of RBC adhesion and important clinical phenotypes, including inflammation and iron overload.

Introduction

Sickle cell disease (SCD) is the most common inherited blood disorder, identified for the first time in the Western world more than 100 years ago.[1] The molecular underpinning of this disease stems from a single point mutation in the β-globin chain of sickle cell hemoglobin (HbS). Replacement of a hydrophilic amino acid, glutamic acid, with valine, a hydrophobic amino acid, in the 6th codon of the β-globin chain results in a variant hemoglobin molecule, HbS, that, when deoxygenated, polymerizes into long chains.[2,3] Intracellular polymerization of HbS results in significant RBC membrane damage and deformation; and may result in lysis of the cell.[4,5] The complexity of SCD can result in a number of clinical manifestations such as stroke,[6,7] pulmonary hypertension,[8] cognitive deficiency,[9] and acute chest syndrome,[10] which further contribute to significant morbidity and mortality in these patients. Healthy human red blood cells (RBCs) have the ability to change their morphology in a reversible manner during oxygen transport. However, HbS-containing RBCs are abnormally stiff and adhesive, and can obstruct the

[a] *Department of Mechanical and Aerospace Engineering, Case Biomanufacturing and Microfabrication Laboratory, Case Western Reserve University, Glennan 616B, 10900 Euclid Ave., Cleveland, OH, USA. E-mail: umut@case.edu; Web: http://www.case-bml.net; Tel: +1 (216) 368-6447*
[b] *Department of Hematology and Oncology, School of Medicine, Case Western Reserve University, Cleveland, OH 44106, USA*
[c] *Seidman Cancer Center at University Hospitals, Case Medical Center, Cleveland, OH, USA*
[d] *Department of Biomedical Engineering, Case Western Reserve University, Cleveland, OH, USA*
[e] *Department of Orthopaedics, Case Western Reserve University, Cleveland, OH, 44106, USA*

† Electronic supplementary information (ESI) available. See DOI: 10.1039/c8ib00004b

microcirculatory flow, leading to episodic painful vaso-occlusive crises (VOC) and contributing to widespread vasculopathy.[11]

Initiation of VOC events in SCD is a multicellular paradigm, likely triggered by aberrant adhesive interactions between RBCs and microvascular bed, and further mediated by impaired RBC biophysical properties.[3,12] In most cases, these events are followed by or simultaneous with the activation of other microcirculatory components, including white blood cells (WBC), platelets, and endothelial cells.[13–17] The interplay between these components, including the collective adhesive events, takes place under a wide spectrum of shear rates determined by the unique geometrical and morphological features of the human microvasculature, as well as by the local changes in the vascular dimensions upon cell–endothelium interactions. The flow conditions may dynamically and continuously change even within the same branch of the microvessel during this entire process.

Recent advances in micro and nano technologies have enabled the fabrication of microfluidic platforms that can recapitulate *in vivo* conditions, at least partially, to examine the key aspects of cellular adhesion at the microscale.[18–20] Utility of these systems have recently revealed molecular, clinical, and biophysical heterogeneity of HbS-containing RBCs[21–25] and their interactions with the microvasculature. Even though these studies contribute significantly to our understanding of cellular adhesion, they do not fully mimic the physiologically relevant flow environment in which shear rates dynamically change in a continuous fashion. Alterations of shear rate in most systems are achieved either by implementation of different pump speeds or through creating branched microfluidic lines with varying dimensions, each having a different flow rate. Both approaches result in discrete shear rate changes and do not recapiculate physiologically continuous shear gradients. Here, we describe a physiologically relevant microfluidic platform (Fig. 1) that generates a shear gradient along the flow direction, in order to investigate the shear dependent adhesion of RBCs at a single flow rate. The microchannel geometry was designed based on the equations derived by Usami *et al.* such that the mean flow velocity and shear stress decreased along the flow direction while the flow rate was maintained constant.[26] Similar microfluidic devices have previously been utilized to study lymphocyte isolation,[27] adhesion of smooth muscle and endothelial cells,[28] as well as label-free CD4+ T cell counting in HIV infected samples.[29] In this paper, we demonstrate the role of such a shear gradient device in describing heterogeneous adhesion of RBCs from subjects with homozygous SCD (HbSS RBCs).

We assessed the shear dependent adhesion of HbSS RBCs to bio-molecules fibronectin (FN) and laminin (LN) using shear gradient microchannels. FN is an adhesive glycoprotein that is found in the extracellular matrix and in plasma as a linker molecule.[30,31] FN has been shown to promote abnormal RBC and WBC (particularly neutrophil) adhesion to the vascular bed in SCD.[32,33] In contrast with FN, LN is embedded inside the sub-endothelial layer and has been implicated in RBC adhesion to the vascular wall in SCD.[34–39] Under normal circumstances, LN is not in contact with flowing blood; however, the endothelial lining retracts in SCD allowing sub-endothelial matrix proteins, including LN, to interact with circulating cells.[34,40] We modeled our shear gradient flow experiments in FN- and LN-immobilized microchannels with a channel height of 50 μm, which is within the scale of physiological range.[41–43] Our results indicate a shear dependent response of RBC adhesion to LN in correlation with subject clinical phenotypes in SCD.

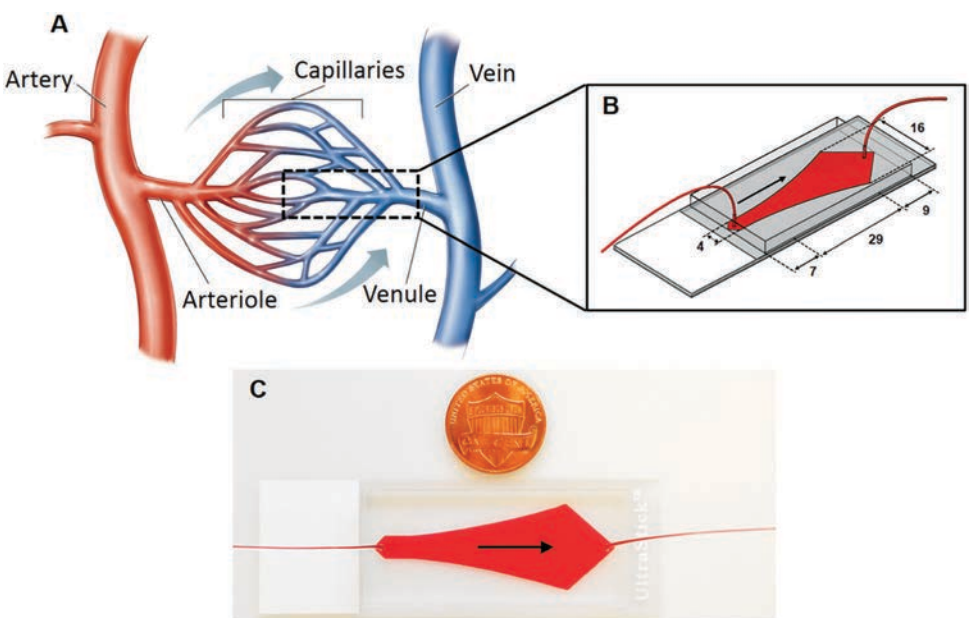

Fig. 1 The shear gradient microfluidic system. Shown is: (A) a schematic representation of the human microcirculatory system, with characteristic shear rates determined by the vessel geometry and local flow conditions. (B) The shear gradient microchannel, in which a shear gradient is formed at a single flow rate. (C) The assembled shear gradient microchannel is shown. Dimensions are in millimeters, and arrows indicate flow direction.

Materials and methods

Live subjects statement

All blood samples, and clinical information about study subjects, such as standard clinical laboratory test results, were obtained following informed consent under the Institutional Review Board (IRB) approval (University Hospitals IRB, Cleveland, OH; IRB number: 05-14-07C). De-identified blood samples were obtained from subjects with homozygous (HbSS) SCD at University Hospitals Adult Sickle Cell Clinic (Cleveland, OH, Division of Hematology and Oncology). All experiments in this study were performed in compliance with the institutional guidelines and with commitment towards the ethical conduct of human subjects research.

Blood samples

Initially, blood samples from consented subjects were drawn into ethylenediaminetetraacetic acid (EDTA)-containing tubes and then aliquoted in 1 mL sealed micro centrifuge tubes while preventing blood exposure to ambient air. A small portion of each sample was sent to the Core Laboratory of University Hospitals Cleveland Medical Center (UHCMC) for High Performance Liquid Chromatography (HPLC) analysis with the Bio-Rad Variant II Instrument (Bio-Rad, Montreal, QC, Canada) to determine the hemoglobin proportions (Hb A, Hb S, Hb F, and HbA2). Subject clinical data including, white blood cell (WBC) count (10^9 L^{-1}), platelet count (10^9 L^{-1}), absolute neutrophil count (ANC) (10^6 L^{-1}), reticulocyte count (10^9 L^{-1}), total hemoglobin (g dL^{-1}), plasma LDH (IU L^{-1}), and ferritin level (μg L^{-1}) were obtained from the Adult Sickle Cell Clinic at UHCMC in Cleveland, Ohio. All experiments in this study were conducted using whole blood samples within 24 hours following venipuncture without any dilution or further processing.

Materials

FN and LN stock solutions (1 mg mL^{-1}) were purchased from Sigma Aldrich (St. Louis, MO, USA). Prior to surface functionalization, both protein solutions were diluted in 1× PBS (pH = 7.4) to have a working concentration of 0.1 mg mL^{-1}. Bovine serum albumin (BSA) was purchased from Sigma Aldrich in a lyophilized powder form and dissolved in 1× PBS at a concentration of 20 mg mL^{-1}. 4-Maleimidobutyric acid *N*-hydroxysuccinimide ester (GMBS) powder was purchased from ThermoFisher Scientific (Waltham, MA, USA). Stock solutions of recombinant human ICAM-1 and VCAM-1 proteins were purchased from Biolegend (San Diego, CA) and diluted to a final concentration of 25 μg mL^{-1} prior to perfusing into the microchannels.

Microchannel fabrication

The microchannels were fabricated by assembling a double sided adhesive (DSA) film on a rectangular polymethyl methacrylate (PMMA) piece and fixing the PMMA onto a functionalized microscope glass slide (Gold Seal, coated with APTES, 3-aminopropyl triethoxysilane, Electron Microscopy Sciences, Hatfield, PA) through the DSA. The adhesive film was micromachined using a laser cutting system (VersaLaser VLS2.30, Universal Laser Systems, Scottsdale, AZ) that defined the microchannel walls. Two identical holes (0.61 mm in diameter) were drilled on the PMMA cap spaced 41 mm from each other to form the inlet and outlet ports using VersaLaser. The microchannel height was determined by the DSA thickness, which was approximately 50 μm and which mimicked the scale of postcapillary venules. The dimensions of the entire channel cross-section is shown in Fig. 1B. Fig. 1C illustrates a macroscopic image of the assembled shear gradient microfluidic device.

Surface functionalization

A cross-linker agent GMBS was used in order to covalently immobilize the endothelium-associated proteins FN and LN to the microchannel surfaces. The stock GMBS solution was obtained by dissolving 25 mg of GMBS in 0.25 mL of dimethyl sulfoxide (DMSO), and it was diluted with pure ethanol to have a final concentration of 0.28% v/v GMBS solution. After assembly, the microfluidic devices were rinsed with PBS (1×) and 100% ethanol. Next, a 60 μL of GMBS working solution was perfused into the channels twice followed by 15 minute incubation in room temperature. The microchannels were then washed with 90 μL of ethanol and PBS twice, then 60 μL of FN, LN, ICAM-1, or VCAM-1 working solutions (100 μg mL^{-1} for FN&LN and 25 μg mL^{-1} for ICAM-1&VCAM-1) were injected into the microchannels and incubated for 1.5 hours at room temperature. In order to prevent non-specific binding, a 90 μL of BSA solution was added into the microchannels, held at 4 °C overnight. Prior to experiments, the microchannels were rinsed with 90 μL of PBS to remove excess BSA.

We characterized the surface coverage of the immobilized proteins – LN and FN – *via* fluorescent labeling. The functionalized microchannels were rinsed with 90 μL of PBS twice to remove unbound BSA solution following the overnight incubation. Next, fluorescently labeled antibody solutions against human LN and FN were loaded into the microchannels, and incubated for 45 minutes. Thereafter, the microchannels were rinsed with PBS twice and the functionalized surface was imaged on an epifluorescent microscope at 10×. The same procedure was carried out with the control surface, which was loaded with PBS excluding LN or FN and incubated with BSA at 4 °C overnight, using the fluorescently labeled antibody solution against human LN. Fig. S1A (ESI†) illustrates the protein coverage in shear-gradient non-functionalized, LN-functionalized, and FN-functionalized microchannels. Quantification of fluorescent intensity, assumed to be the indicative of the amount of immobilized protein, shows negligible background fluorescence on the control surface and reveals protein coverage over the functionalized surfaces (Fig. S1B, ESI†).

Blood processing and data acquisition

The microchannels were placed on an Olympus IX83 inverted motorized microscope stage for visualization following the assembly of inlet tubings. Next, 300 μL of blood in a 1 mL syringe was connected to a constant displacement syringe pump (New Era NE-300, Farmingdale, NY). Blood was perfused into the microchannels at a constant flow rate of 28.5 μL min^{-1} until they were completely filled. Afterwards, the flow rate was decreased to 1.85 μL min^{-1}, corresponding to an approximate shear stress

of 1 dyne cm^{-2} at the smallest cross section of the microchannel, and 45 μL of blood was injected at this flow rate. In order to wash the non-adherent cells off the microchannel surfaces, a new syringe containing 1 mL of wash buffer containing 1% BSA and 0.09% sodium azide was connected to the device and the buffer was pumped at a constant flow rate of 40 μL min^{-1} corresponding to a mean velocity of 200 mm min^{-1} at the smallest section of the converging cross-section. The buffer solution was allowed to perfuse until all non-adherent cells were completely cleared out of the microchannels. Next, the phase-contrast images of the microchannel surfaces with the adherent cells were recorded at 20× using the Olympus Cell Sense live imaging software. Post processing of recorded images and cell counting were performed using Adobe Photoshop CS5 (San Jose, CA, USA).

Results and discussion

Computational analysis of the fluid flow in the shear gradient microchannel

Numerical simulations were performed by a commercially available finite element analysis (FEA) software package COMSOL 4.3 (Burlington, MA) to characterize the velocity and shear rate profiles in the shear gradient microchannels using a 3D model. A structured mesh was created with a total number of 45120 hexahedral elements throughout the entire domain. The buffer fluid was modeled as Newtonian with a dynamic viscosity and density of 0.001 Pa s and 993 kg m^{-3} [21] respectively. The inlet boundary condition was set to "Velocity Inlet" with a calculated average velocity of 26.7 mm s^{-1} from the volumetric flow rate and tubing dimensions. The outlet pressure was set to 0 as the buffer discharged to the atmospheric pressure. The Reynolds number inside the microchannel was computed using the equation below:

$$\mathrm{Re} = \frac{\rho Q h}{\mu A} \quad (1)$$

where ρ is the fluid density, Q is the volumetric flow rate, h is the characteristic length (channel height), μ is the dynamic viscosity of the fluid, and A is the cross sectional area. The Re number at the inlet (where the width of the microchannel is 4 mm) was approximately 0.2, indicating that the flow regime was predominantly in the laminar region. Fig. 2 illustrates a 2D representation

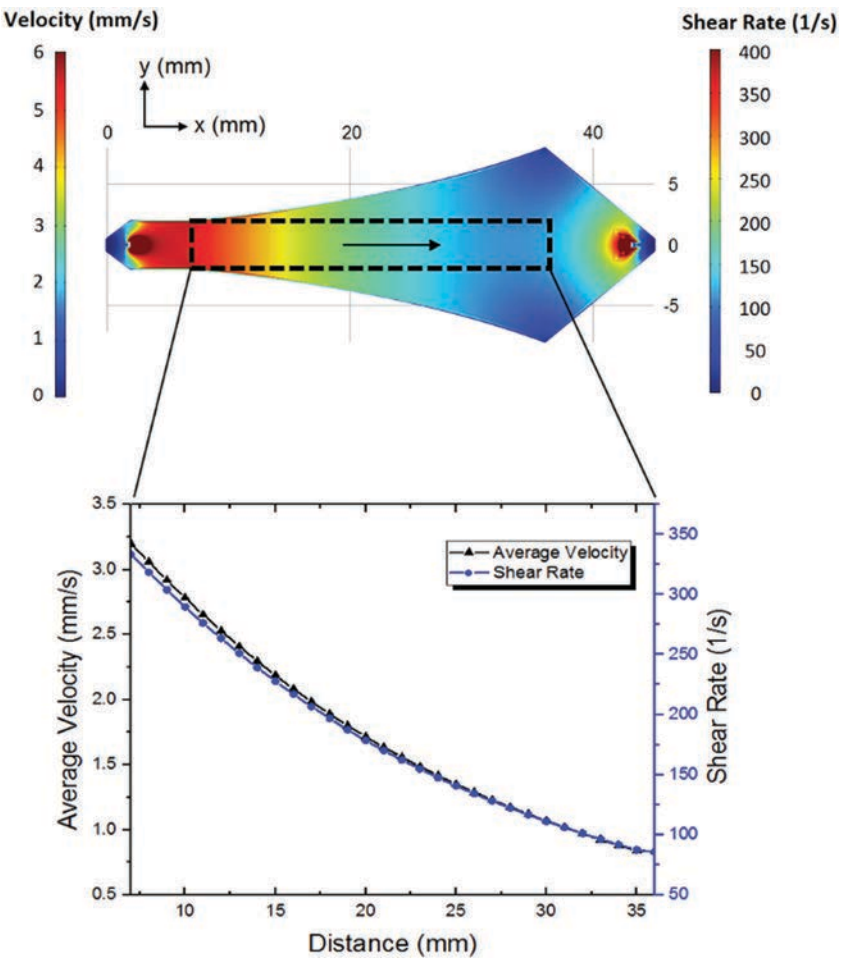

Fig. 2 Flow velocity and shear rate contours on a 2D plane 5 μm above the microchannel bottom surface. Shown is the region of interest (ROI, dashed line) in which the data analyses were performed. As shown graphically, there is a 3-fold reduction in average velocity and shear rate through the defined ROI. Arrow indicates flow direction.

of the velocity and shear rate distributions along the microchannel. In order to mimic the local flow conditions in the vicinity of the adherent cells, the numerical results were evaluated on a plane that was positioned 5 μm above the microchannel bottom surface.

Total RBC adhesion depends on the change of shear rate gradient

We analyzed the shear dependent adhesion characteristics of HbSS RBCs to LN and FN in a shear gradient environment. Based on the numerical simulations, we chose a rectangular region of interest (ROI) for experimental data analysis as shown in Fig. 2. Next, we divided each ROI into 10 identical sub-regions and quantified the mean shear rates for individual sub-regions using COMSOL (Fig. 3A). Then, we correlated the number of adherent cells in each sub-region with the corresponding mean shear rate. Fig. 3A and B are visual representations of the adherent RBCs in LN immobilized shear constant (straight rectangular channel) and shear gradient channels respectively for a single subject with SCD. The shear constant channel was fabricated using the same technique, but having a constant width corresponding to the inlet width of the shear gradient channel (w = 4 mm). Fig. 3A and B represent the ROIs defined earlier (Fig. 2) and the red dots illustrate the individual adherent RBCs (not to scale). Fig. 3C shows the variation in number of RBCs attached to LN within individual sub-regions. The adherent cells did not change across the shear constant channel and homogeneously distributed along the functionalized microchannel surface. In the shear gradient microchannel, however, RBC adhesion was enhanced at low shear by >2-fold relative to the first sub-region. In the first two sub-regions, where the mean shear rates did not differ significantly, the adhesion rates were comparable. We observed more than 1.5-fold increase in average RBC adhesion throughout the ROI in the shear gradient microchannel (Fig. 3C).

Fig. 4 shows the average adhesion curves for control (non-SCD, healthy individuals, HbAA) and HbSS samples in LN functionalized microchannels. The HbAA samples displayed negligible

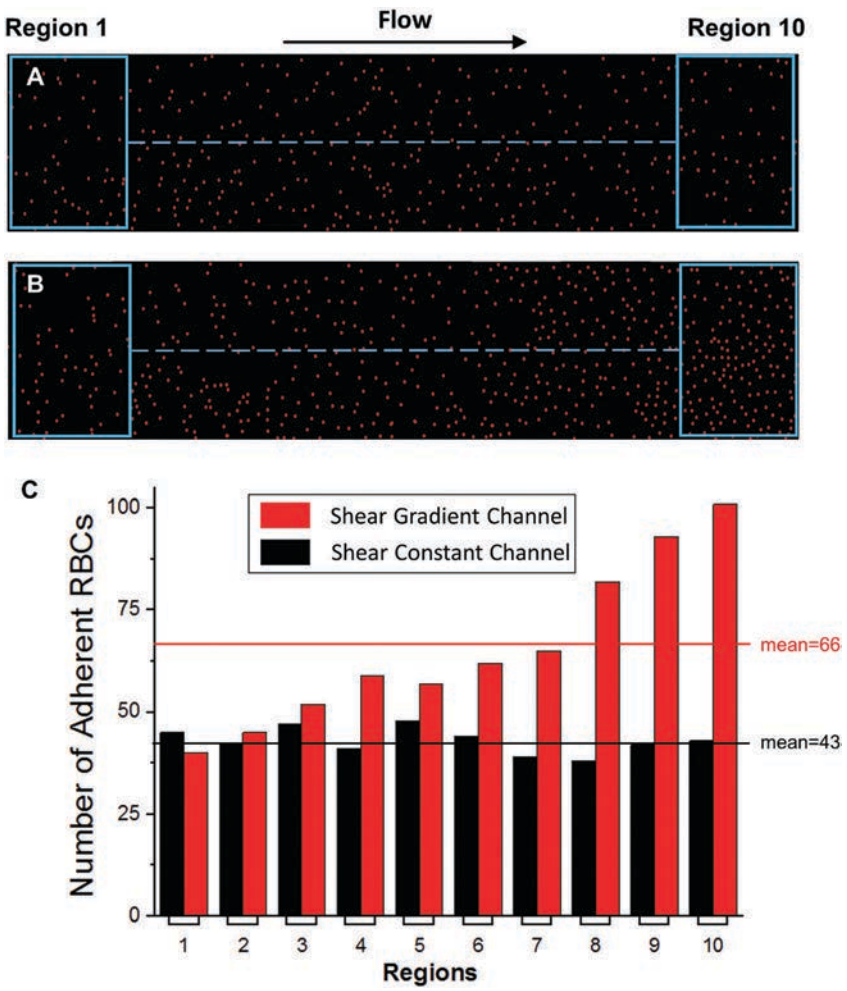

Fig. 3 Shear gradient adhesion of RBCs. Shown is (A) HbSS RBCs after passage through a shear constant microchannel, with little variation in adhesion seen across the ROI. (B) Adherent cells across the shear gradient microchannel, in which adhesion increases with decreasing shear rates. (C) Quantification of adherent HbSS RBCs across shear constant–shear gradient microchannels. The overall difference between the means was more than 50% (p = 0.002, one-way ANOVA). Blue rectangles in (A) and (B) represent the individual sub-regions.

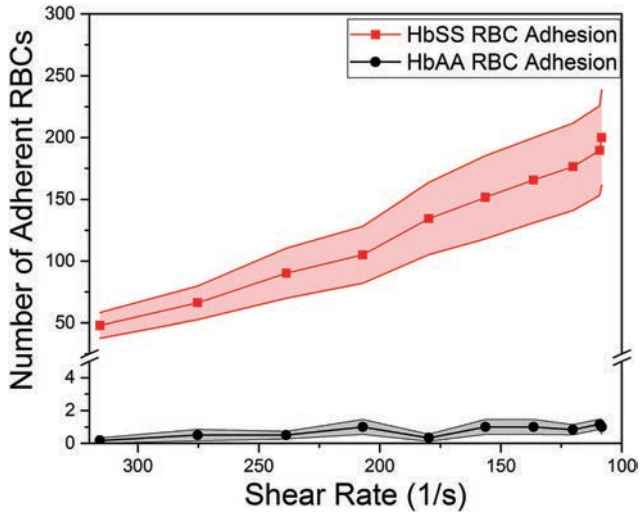

Fig. 4 The average shear dependent adhesion curves for subjects with HbAA (n = 6) and HbSS (n = 20) in LN functionalized microchannels. Adhesion of HbSS RBCs declines with increasing shear rates whereas HbAA-containing RBCs do not exhibit significant shear-dependent adhesion with very low overall adhesion numbers. The shaded areas represent ± standard error of the mean (SEM).

RBC adhesion to LN with no significant correlation between shear rate and number of adherent RBCs (n = 6). HbSS RBCs adhered to LN with a shear-dependent profile showing a more than 3-fold increase in average adherent RBC numbers throughout the ROI.

To ensure that the concentration of flowing cells did not significantly change across the width of the microchannel from region 1 to region 10, which may affect the number of adherent cells in each region, we developed a CFD model to evaluate the variation in RBC distribution within the ROI (Video S1, ESI†). We carried out a computational study of the 3D particle flow to simulate the motion of RBC-sized spherical particles through the shear-gradient microchannel. 3D transient numerical study for the particle flow was performed using COMSOL 4.3 by introducing spherical particles with a diameter of 3 μm to simulate flowing RBCs. Initial particle velocities were adjusted based on the flow field at the inlet. A total number of 2000 particles were released every 0.1 s for a total simulation duration of 40 seconds, at which the flow reached steady-state. The particle density was set to 1.1 g mL^{-1}, simulating the average density of an individual RBC.[44] Video S1 (ESI†) displays the motion of flowing particles through the shear-gradient microchannel and change of particle concentration as the flow becomes steady-state. In the beginning, the particles are more dilute towards downstream due to continuously introduced particles at the inlet. Nonetheless, particle concentration becomes more consistent as the flow progresses and reaches a steady state approximately 40 seconds after flow has been started (Fig. S2A, ESI†). At steady state, particle concentration was consistent throughout the sub-regions of the ROI, with 5.4% to 7.8% variation of the mean (Fig. S2B, ESI†).

We further performed experimental analyses in order to validate our computational simulations. We utilized the grayscale intensities of the phase-contrast microscopic images to approximate the hematocrit (Hct) value in each sub-region (Fig. S3A, ESI†). When the microchannels were loaded with isolated RBCs (100% Hct), the grayscale intensity levels were significantly lower and remained rather consistent throughout the ROI (Fig. S3B, ESI†). Flowing blood samples at hematocrits of 10% and 20% produced higher grayscale intensities caused by reflections from brighter RBCs relative to dark background in the phase-contrast mode. However, further increase in Hct (50–100%) led to diminished transparency of the flow area and thus lower grayscale intensities. We observed intensity levels similar to those of 50% Hct upon perfusing a whole blood sample, and the intensity levels displayed a slight increase near the outlet suggesting that RBCs were more dilute in those regions. Nevertheless, the difference was small enough to negate any dilution effect on RBC adhesion between regions, which was consistent with the numerical findings. Further, we use undiluted and pre-processing free whole blood samples, ensuring that sufficient number of RBCs are in contact with the microchannel surface during perfusion.

Fig. 5 shows typical distributions of adherent HbSS RBCs with varying shear rates from a single sample in LN and FN functionalized channels. Deformable and non-deformable RBCs were previously defined in our publications.[21,45,46] We have previously shown that non-deformable RBCs have a characteristic elongated shape and permanently lack their characteristic biconcave morphology in normal oxygen conditions.[21,46] Adherent HbSS RBCs can be visually identified as deformable or non-deformable based on their morphology, including their shape and aspect ratio. HbSS RBCs undergo repeated sickling–unsickling events due to the changing oxygen levels throughout the circulation, where their morphology and deformability significantly alter in a cyclic manner.[47,48] These repeated events eventually result in permanent impairment in RBC shape and deformability (*i.e.* irreversibly sickled RBCs), creating a heterogeneous RBC subpopulation,[47] which we have thoroughly characterized in terms of adhesion and deformability in our earlier work.[21,46] Illustrations of deformable and non-deformable RBCs are included in Fig. 5A for LN and Fig. 5B for FN.

To assess the extent to which individual RBC subpopulations responded to the shear rate gradient, we fitted linear regression curves for both deformable and non-deformable RBC adhesion data (Fig. 5), and observed a significantly greater deformable RBC adhesion rate in LN immobilized microchannels in comparison to FN microchannels for the sample tested. Moreover, deformable RBC adhesion to LN was highly shear dependent, showing a more than 3-fold increase in adherent cell numbers between region 1 and region 10. In order to quantify the shear dependent adhesion of individual samples, the absolute value of the slope of the curves was defined as ''RBC Shear Gradient Microfluidic Adhesion (SiGMA) index'', in which a lower SiGMA index suggests greater adhesion under higher shear rates. The linear regression curves and corresponding regression equations were generated in OriginLab (Northampton, MA) for all the samples tested. Negative slopes in Fig. 5 indicate declining adhesion with increasing shear rate. A graphical illustration of SiGMA index is shown in Fig. 6.

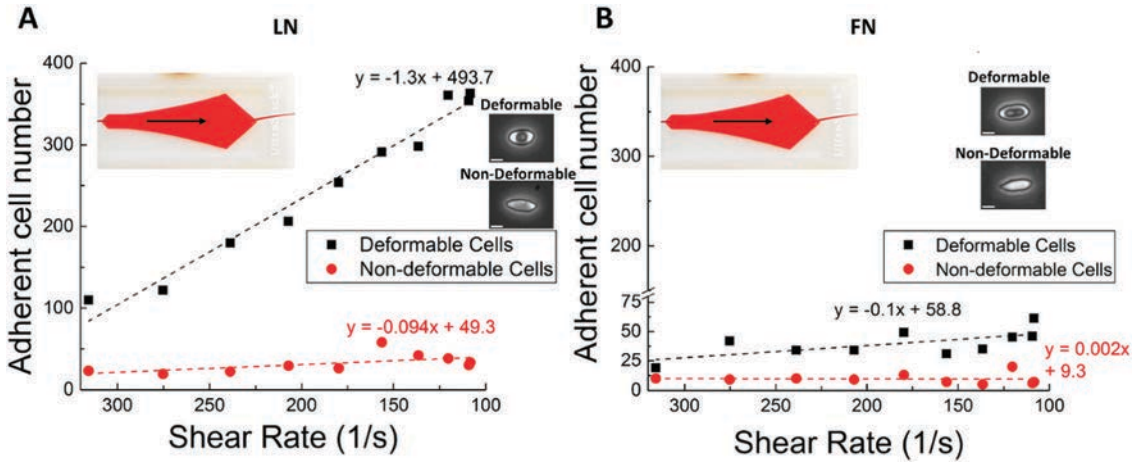

Fig. 5 Sample distribution of adherent deformable and non-deformable cell numbers in LN and FN functionalized microchannels across shear gradient channel. Shown are linear fitted curves (dashed lines) and the corresponding equations used to quantify shear dependent adhesion data in LN (A) and FN (B) functionalized channels, such as the slope, from a single subject. The microchannel images are shown at top left corners to illustrate direction of the flow. Appearance of deformable and non-deformable RBCs are illustrated for each adhesion type. Scale bars are 5 μm.

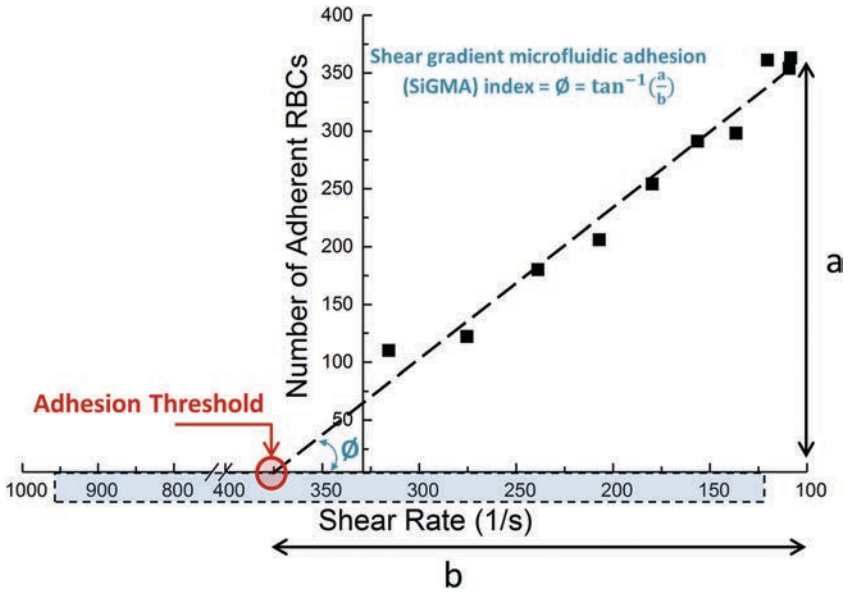

Fig. 6 Parameters defined to quantify shear dependent RBC adhesion. The data points are obtained from a single subject and represent the total RBC adhesion to LN. The dashed line is fitted through linear regression and extended above the maximum shear rate used in the study (~310 s^{-1}) to determine the predicted shear value above which adhesion took place, which was defined as "adhesion threshold". Normalized RBC shear gradient microfluidic adhesion (nSiGMA) index was calculated in the same fashion as SiGMA index, with the difference being the slope was determined based on normalized RBC adhesion numbers. The shaded region encompasses the typical physiological shear rate range for post capillary venules.

Determination of SiGMA index using shear gradient microfluidic channels

The calculated SiGMA indices for a group of SCD subjects are shown in Fig. 7A. Deformable RBC adhesion to LN was significantly more shear dependent, compared with non-deformable RBC adhesion to LN, as well as deformable and non-deformable RBC adhesion to FN ($p < 0.01$, one-way ANOVA). The influence of shear rate may be minimized in relatively low-adhesion samples, where low absolute numbers of adherent RBCs negate the effect of shear rate. Therefore, we normalized the SiGMA index based on RBC adhesion in the first sub-region of the entire ROI, by computing the normalized adhesion numbers for each sub-region and generated normalized adhesion curves using the equation below:

$$\text{Normalized adhesion number} = \frac{\text{Number of adherent RBCs in a subregion}}{\text{Number of adherent RBCs in first subregion}} \times 100 \quad (2)$$

Next, we defined the slope of each normalized adhesion curve as normalized Shear Gradient Microfluidic Adhesion (nSiGMA) index. Eqn (2) was used to determine the percent increase in

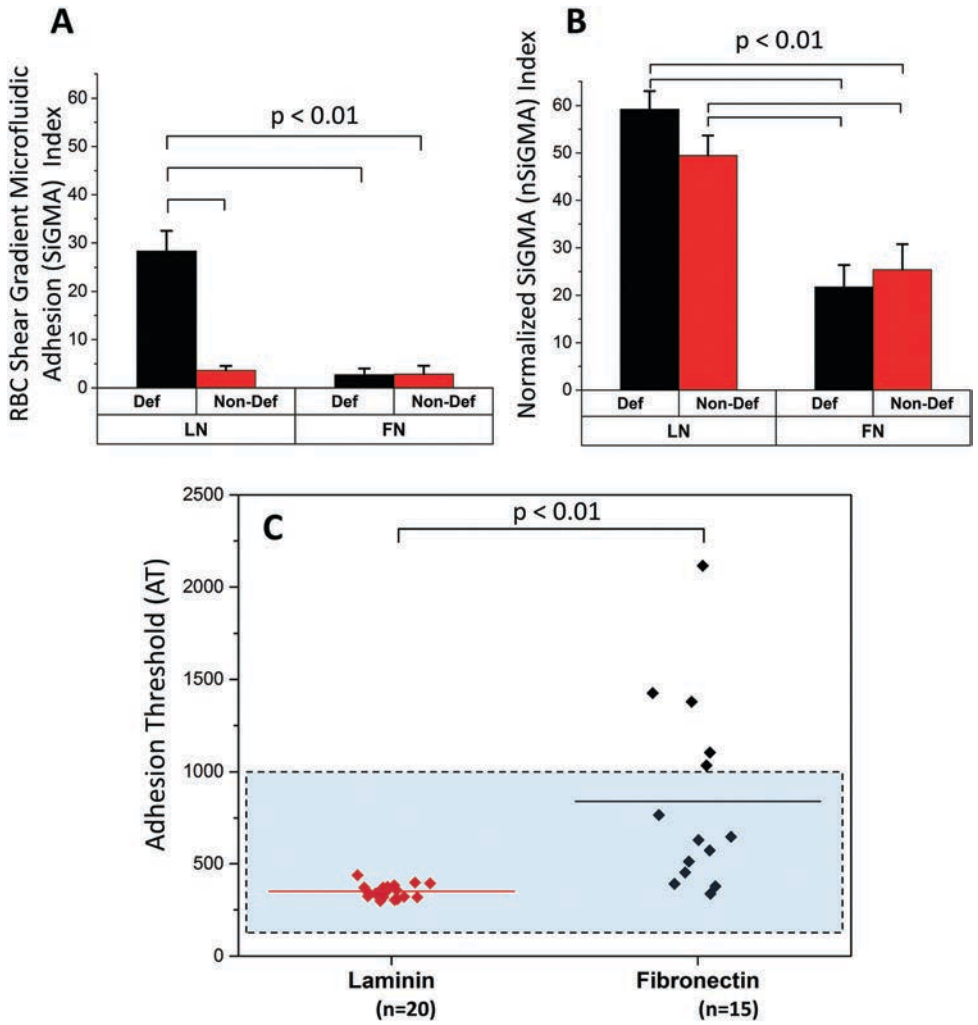

Fig. 7 Shear dependent deformable and non-deformable HbSS RBC adhesion to LN & FN is heterogeneous. Shown are calculated RBC SiGMA indices (absolute slope) for (A) raw data and (B) normalized data for deformable and non-deformable RBC adhesion in LN and FN functionalized microchannels. (C) Shown is the calculated "adhesion threshold" where cells are projected to no longer adhere. The blue dashed line represents a typical range of post-capillary shear rates between 112 s^{-1} and 952 s^{-1}. The horizontal brackets between the individual groups show statistically significant difference based on a one-way ANOVA test with Tukey's *post hoc* test for multiple comparisons ($p < 0.01$).

adherent RBC numbers in a specific sub-region compared to the first sub-region. Hence, the influence of total adherent cell numbers on SiGMA index calculations was negated, which allowed comparison of low- and high-adhesion samples. Fig. 7B shows that there was difference in SiGMA indices between HbSS RBC adhesion to LN or FN ($p < 0.01$, one-way ANOVA). Although the deformable cells displayed increased nSiGMA indices, we did not observe a significant correlation between the two RBC subpopulations. Fig. S4 and S5 (ESI†) illustrate the individual adhesion curves, from which the SiGMA and nSiGMA indices were calculated, for each SCD sample along with a HbAA control group.

Deformable and non-deformable HbSS RBCs had different responses to changes in shear rate. The calculated SiGMA indices indicated that deformable RBCs were more shear dependent than non-deformable ones. In other words, deformable cells were more sensitive to changes in shear rate and could be removed to a significantly greater extent with increasing shear rates. However, this behavior might have been amplified due to the high number of adherent RBCs to LN. Calculated nSiGMA indices revealed that adhesion of both deformable and non-deformable RBCs to LN was more shear dependent than adhesion to FN, as shown in Fig. 7B, and, we did not observe a significant difference between shear dependent responses by deformable and non-deformable RBCs. In general, FN-adherent RBCs did not respond to the shear gradient and maintained persistent attachment with an approximate nSiGMA value of 20 (Fig. 7B). A high rate (elevated slope) of shear dependent adhesion implied a tendency of adherent RBCs to detach relatively easily at high shear sites in the microchannel, whereas lower shear dependency corresponded to more persistent RBC adhesion, which might not be influenced as much by elevated shear rates.

Adhesion threshold in FN-functionalized microchannels reveals persistent RBC adhesion beyond the physiological limits

In addition to SiGMA and nSiGMA indices described herein, we further calculated the *x*-axis intercept of the regression

curves obtained for each sample, which was defined as the adhesion threshold, as illustrated in Fig. 6. The intercept point represented the predicted shear rate required to remove all of the adherent RBCs (deformable and non-deformable) from LN or FN. Therefore, an increased adhesion threshold implied that adherent RBCs would persist at high shear rates. As shown in Fig. 7C, the estimated mean adhesion threshold for HbSS RBCs adherent to LN was 351 s^{-1}. All adhesion threshold values were within a physiological shear range of 121 s^{-1} (minimum) and 952 s^{-1} (maximum), typical for post-capillary venules.[49] The mean adhesion threshold for FN adherent cells was 839 s^{-1}, with 5 subjects having adhesion thresholds above the phsyiological range. Our data indicated that more attachment–detachment events may take place in a LN functionalized microchannel for a given SCD subject, yet the physiological shear rates could prevent a persistent RBC attachment in the system. On the other hand, FN-adherent RBCs, despite fewer absolute attachments, may remain attached for longer periods of time when exposed to physiological shear rates.

Shear dependent RBC adhesion associates with clinical phenotype in SCD

We have observed a heterogeneous response of adherent RBCs to the shear gradient as indicated by several parameters namely: SiGMA, nSiGMA, and adhesion threshold. This heterogeneity exists both at the individual SCD subject level and in the population. Therefore, we investigated potential associations between adhesion data and clinical phenotypes in SCD. Fig. 8 shows the association of several clinical parameters based on nSiGMA indices for LN. We separated the study population into two groups based on a nSiGMA of 60 (Table 1). The adherent cell numbers represent the summation of both deformable and non-deformable RBCs. The statistical analyses were carried out with Minitab 17 (Minitab, State College, PA) software package. The data were analyzed using analysis of variance (ANOVA) with Tukey's *post hoc* test for multiple comparisons and the p value for each dataset reported (Fig. 8). Subjects with low response to shear dependent adhesion to LN (*i.e.* less reduction of adhesion with increasing shear rates, lower nSiGMA) displayed elevated levels of WBC, ANC, and ferritin

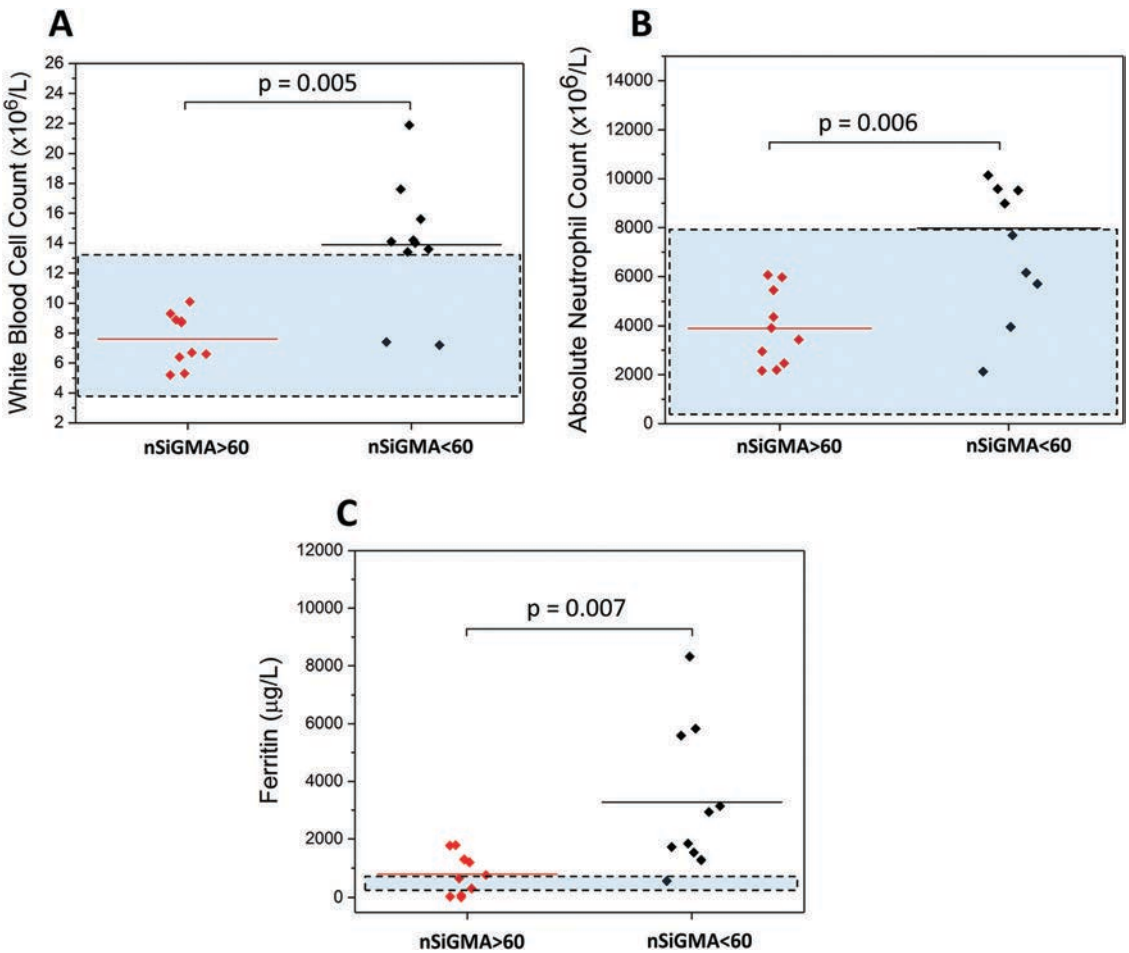

Fig. 8 Shear dependent adhesion of HbSS RBCs to LN and clinical parameters. Shear dependent adhesion was lower (nSiGMA) in subjects with (A) an elevated white blood cell (WBC) count, (B) an elevated absolute neutrophil count (ANC), and (C) ferritin. The dashed regions show the typical ranges in healthy individuals. The horizontal bracket lines between the two groups represent statistically significant difference based on a one-way ANOVA test with Tukey's *post hoc* test for multiple comparisons. The total number of subjects was 10 for each group.

Table 1 Clinical phenotype of the study population based on their shear dependent adhesion characteristics

	High shear dependent adhesion (nSiGMA > 60) (mean ± st. err.)	Low shear dependent adhesion (nSiGMA < 60) (mean ± st. err.)	Range	*P*-value[a]
Age	33.9 ± 4.57	30.4 ± 1.89	21–61	0.488
Hgb (g dL^{-1})	8.54 ± 0.49	7.35 ± 0.62	2.6–10.7	0.149
WBC (10^9 L^{-1})	**7.6 ± 0.56**	**13.9 ± 1.37**	**5.2–21.9**	**0.005**
ANC (10^6 L^{-1})	**3898 ± 479.4**	**7979 ± 1215**	**2130–15 930**	**0.006**
Platelet count (10^9 L^{-1})	330.8 ± 60.1	353.7 ± 24.07	174–781	0.728
Reticulocyte count (10^9 L^{-1})	248.4 ± 20.77	408.6 ± 75.24	122–813	0.055
Lactate dehydrogenase (U L^{-1})	363.3 ± 61.68	518 ± 72.75	154–813	0.122
Ferritin (μg L^{-1})	**784.5 ± 219.62**	**3272.3 ± 791.9**	**11–8320**	**0.007**
Hemoglobin S (%)	73.48 ± 6.69	59.96 ± 6.45	27.2–91	0.190
Hemoglobin A (%)	13.22 ± 7.29	26.85 ± 6.32	1.4–66.8	0.206
Hemoglobin F (%)	7.05 ± 1.95	3.89 ± 1.34	0.7–18.1	0.240

A total of 20 blood samples (*n*) were obtained from 20 subjects (male = 10, female = 10). All subjects are homozygous HbSS. WBC: white blood cell count, ANC: absolute neutrophil count. [a] Based on ANOVA one-way test.

(Fig. 8A–C, *p* values are 0.005, 0.006, and 0.007 respectively, one-way ANOVA).

Inflammatory cells play a critical role in initiating vaso-occlusive crises and contribute to the pathophysiology of SCD in various ways.[32,50] Here, we show that SCD subjects with high WBC counts exhibit lower shear dependent RBC adhesion characteristics to LN, with the implication that RBC attachment in these subjects is stronger and more resistant to high shear rates for cell detachment (Fig. 8A). We have also observed a similar behavior with absolute neutrophil counts (ANC) (Fig. 8B) in accordance with an earlier study that reported a correlation between peripheral neutrophil count and clinical severity of SCD.[51] Lard *et al.* (1999) reported that neutrophils are highly activated in subjects with SCD particularly during vaso-occlusive events.[52] Neutrophil activation in SCD could be triggered by various chemokines present in blood serum such as interleukin-8 (IL-8), sickled RBC-dependent IgG-enhanced as well as complement activation pathways, and activated endothelial line.[53–55] It has previously been shown that activation of HbSS RBCs by IL-8 induced RBC adhesion to the endothelium enhanced by FN.[56] Here, our findings indicate that absolute number of neutrophils may also play a role in mediating the adhesion strength of RBCs to LN, which could indicate a novel pathway for neutrophils to contribute to severity of the disease. Further studies are required to unearth the mechanism underlying the association between neutrophils and shear dependent RBC adhesion.

Patients with SCD on chronic and prolonged RBC transfusion therapy are likely to suffer from iron overload that can lead to serious complications and even higher mortality rates.[57–60] Therefore, it's critical to accurately monitor the states of iron overload of such patients. Serum Ferritin (SF) is one of the most common clinical tests in determining iron overload that provides adequately reliable results.[61–64] In addition to the clinical implications of iron overload in SCD, we have shown that increased SF levels are inversely proportional with the shear dependent adhesion of RBCs to LN (Fig. 8C). Hence, it could be speculated that presence of excessive intracellular iron levels helps enhance the adhesion strength of HbSS RBCs to LN. Alternatively, RBCs from subjects with more severe disease (requiring transfusion) may exhibit lower nSiGMA.

Earlier studies by R. P. Hebbel and N. Mohandas revealed that HbSS RBC adhesion to the endothelium correlates with clinical severity in subjects with SCD.[65–67] Since then, a number of groups have sought to identify different pathways whereby RBCs take part in the initiation of VOC events. In addition to LN and FN, other endothelial-associated proteins have been found to mediate HbSS RBC adhesion, including VCAM-1, P-Selectin, Thrombospondin (TSP), and $\alpha v\beta 3$ integrin.[68–73] Moreover, plasma factors have also been shown to facilitate HbSS RBC adhesion by forming bridges between RBC surface receptors and endothelial- or platelet-associated ligands, such as TSP and vWF.[74–76] Further, WBCs with an activated phenotype contribute to the pathophysiology of SCD *via* creation of a highly thromboinflammatory milieu.[14,50,77] Adhesion of activated WBCs to vascular endothelium stimulates the expression of adhesion molecules and mediates the interplay between different cell types, including platelets.[78] Accelerated RBC lysis and resultant increased extracellular heme levels also induce endothelial activation and facilitate the emergence of a procoagulant environment through the formation of neutrophil extracellular traps (NETs).[79–81] Therefore, a thorough investigation of SCD must, in addition to abnormal RBC adhesion to various endothelial proteins, incorporate the study of all individual contributors of SCD pathogenesis, including WBCs, platelets, and ECs, and the interplay between them. However, our work is not a comprehensive survey of shear-dependent adhesion of HbSS RBCs to all endothelium proteins identified to mediate RBC adhesion, nor is it meant to interrogate all possible cellular adhesion events in SCD. Rather, the shear-gradient microfluidic channel presented here holds great promise as a tool through which to evaluate, qualitatively and quantitatively, abnormal adhesion of HbSS RBCs to a range of endothelial proteins as well as intact endothelial cells, and to assess adhesion and activation of WBCs, platelets, and ECs in physiologically relevant shear flow conditions. Our preliminary findings, from 3 subjects with SCD, suggest shear-dependent adhesion characteristics of sickle RBCs in laminin, fibronectin, ICAM-1, and VCAM-1 functionalized microchannels (Fig. S6A, ESI†). We did not observe any significant adhesive interactions between RBCs with HbAA and these adhesive molecules immobilized in the microchannels as shown in Fig. S6B (ESI†).

Conclusions

In conclusion, this study examined the shear dependent adhesion of HbSS RBCs to LN and FN in a microfluidic platform, in which the shear gradient was imposed based on the microchannel geometry along the flow direction. The shear gradient flow was continuous and driven by a single pump at a constant flow rate. One of the major findings of this work was the heterogeneous adhesive response of HbSS RBCs to a shear gradient when interacting with adhesion proteins LN or FN. The manifestation of this heterogeneity differed significantly between LN- and FN-adherent RBCs. We speculate that FN-adherent RBCs have higher adhesion strength compared to LN-adherent RBCs, preventing detachment at high shear rates. Indeed, we observed a higher non-deformable to deformable RBC adhesion ratio in FN-functionalized microchannels, which supports our previous findings describing a relatively higher adhesion strength of these RBCs.[21,45]

Based on shear dependent adhesion analyses, we reported new subject-specific and clinically-relevant parameters: RBC Shear Gradient Microfluidic Adhesion (SiGMA) index, RBC normalized Shear Gradient Microfluidic Adhesion (nSiGMA) index, and adhesion threshold (AT) values, which may help describe the dynamic pathophysiology of SCD and role of shear rate in vaso-occlusion. We observed a significant subject-dependent variation of AT for FN microchannels as opposed to LN, which could also be attributed to the high rate of persistently-adhered non-deformable RBCs to FN. Moreover, our findings suggest a link between nSiGMA and clinical phenotypes of inflammation and iron overload in subjects with SCD, lower nSiGMA associating with worse outcome (Table 1). Ultimately, better understanding of the adhesion phenomenon in SCD requires the interrogation of RBC, WBC and platelet adhesion to a wide range of endothelium proteins (such as ICAM-1, VCAM-1, P-Selectin, and E-Selectin) and the interactions between them, which synergistically trigger VOC events in the microvasculature. Our physiologically relevant approach, as presented here, has the potential to analyze these important interactions, which we will incorporate in future studies. This study paves the way for shear-dependent interrogation of cellular adhesion to a wide spectrum of biologically relevant substrates, including (sub)-endothelium proteins as well as endothelial cells, which may lead to improved clinical monitoring and development of novel therapeutic targets.

Author contributions

E. K., J. A. L., and U. A. G. developed the idea and designed the experiments. E. K. performed the experiments, E. K., J. A. L. and U. A. G. analyzed the results, E. K., J. A. L., and U. A. G. prepared the figures, the ESI,† and wrote the manuscript.

Conflicts of interest

There are no conflicts to declare.

Acknowledgements

This work was supported by grant #2013126 from the Doris Duke Charitable Foundation, National Heart Lung and Blood Institute R01HL133574, and National Science Foundation CAREER Award 1552782. U. A. Gurkan acknowledges the Case Western Reserve University, University Center for Innovation in Teaching and Education (UCITE) for the Glennan Fellowship, which supports the scientific art program and art student internship in Case Biomanufacturing and Microfabrication Laboratory. The authors acknowledge with gratitude the contributions of subjects and clinicians at Seidman Cancer Center (University Hospitals, Cleveland). Authors would like to thank Grace Gongaware from Cleveland Institute of Art for her scientific illustrations used in this work.

References

1 J. B. Herrick, *Yale J. Biol. Med.*, 2001, **74**, 179–184.
2 D. C. Rees, T. N. Williams and M. T. Gladwin, *Lancet*, 2010, **376**, 2018–2031.
3 D. K. Wood, A. Soriano, L. Mahadevan, J. M. Higgins and S. N. Bhatia, *Sci. Transl. Med.*, 2012, **4**, 123ra126.
4 F. A. Kuypers, *Hematol. Oncol. Clin. North Am.*, 2014, **28**, 155–179.
5 R. P. Hebbel, *Blood*, 1991, **77**, 214–237.
6 L. A. Verduzco and D. G. Nathan, *Blood*, 2009, **114**, 5117–5125.
7 M. Talahma, D. Strbian and S. Sundararajan, *Stroke*, 2014, **45**, e98–100.
8 G. H. Fonseca, R. Souza, V. M. Salemi, C. V. Jardim and S. F. Gualandro, *Eur. Respir. J.*, 2012, **39**, 112–118.
9 C. Andreotti, A. A. King, E. Macy, B. E. Compas and M. R. DeBaun, *J. Child Neurol.*, 2015, **30**, 1349–1353.
10 K. Pahl and C. A. Mullen, *Exp. Biol. Med.*, 2016, **241**, 745–758.
11 J. B. Caboot and J. L. Allen, *Paediatr. Respir. Rev.*, 2014, **15**, 17–23.
12 P. S. Frenette, *Curr. Opin. Hematol.*, 2002, **9**, 101–106.
13 J. Villagra, S. Shiva, L. A. Hunter, R. F. Machado, M. T. Gladwin and G. J. Kato, *Blood*, 2007, **110**, 2166–2172.
14 J. D. Belcher, P. H. Marker, J. P. Weber, R. P. Hebbel and G. M. Vercellotti, *Blood*, 2000, **96**, 2451–2459.
15 A. A. Solovey, A. N. Solovey, J. Harkness and R. P. Hebbel, *Blood*, 2001, **97**, 1937–1941.
16 A. Solovey, Y. Lin, P. Browne, S. Choong, E. Wayner and R. P. Hebbel, *N. Engl. J. Med.*, 1997, **337**, 1584–1590.
17 Y. Alapan, A. Fraiwan, E. Kucukal, M. N. Hasan, R. Ung, M. Kim, I. Odame, J. A. Little and U. A. Gurkan, *Expert Rev. Med. Devices*, 2016, **13**, 1073–1093.
18 H. Lu, L. Y. Koo, W. M. Wang, D. A. Lauffenburger, L. G. Griffith and K. F. Jensen, *Anal. Chem.*, 2004, **76**, 5257–5264.
19 K. R. Partola, B. Andemariam and G. Lykotrafitis, *J. Mech. Behav. Biomed. Mater.*, 2017, **71**, 80–84.
20 Y. Alapan, K. Icoz and U. A. Gurkan, *Biotechnol. Adv.*, 2015, **33**, 1727–1743.

21 Y. Alapan, J. A. Little and U. A. Gurkan, *Sci. Rep.*, 2014, **4**, 7173.
22 X. Li, E. Du, H. Lei, Y. H. Tang, M. Dao, S. Suresh and G. E. Karniadakis, *Interface Focus*, 2016, **6**, 20150065.
23 D. K. Kaul, M. E. Fabry, P. Windisch, S. Baez and R. L. Nagel, *J. Clin. Invest.*, 1983, **72**, 22–31.
24 D. K. Kaul, R. L. Nagel and S. Baez, *Microvasc. Res.*, 1983, **26**, 170–181.
25 D. K. Kaul, M. E. Fabry and R. L. Nagel, *Blood*, 1986, **68**, 1162–1166.
26 S. Usami, H. H. Chen, Y. Zhao, S. Chien and R. Skalak, *Ann. Biomed. Eng.*, 1993, **21**, 77–83.
27 S. K. Murthy, A. Sin, R. G. Tompkins and M. Toner, *Langmuir*, 2004, **20**, 11649–11655.
28 B. D. Plouffe, D. N. Njoka, J. Harris, J. Liao, N. K. Horick, M. Radisic and S. K. Murthy, *Langmuir*, 2007, **23**, 5050–5055.
29 X. Cheng, D. Irimia, M. Dixon, K. Sekine, U. Demirci, L. Zamir, R. G. Tompkins, W. Rodriguez and M. Toner, *Lab Chip*, 2007, **7**, 170–178.
30 J. Xu and D. Mosher, in *Biology of Extracellular Matrix*, ed. R. P. Mecham, Springer, Berlin Heidelberg, 2010, ch. 2, pp. 41–75.
31 W. S. To and K. S. Midwood, *Fibrog. Tissue Repair*, 2011, **4**, 21.
32 M. R. Kasschau, G. A. Barabino, K. R. Bridges and D. E. Golan, *Blood*, 1996, **87**, 771–780.
33 E. R. Burns, W. H. Wilkinson and R. L. Nagel, *J. Lab. Clin. Med.*, 1985, **105**, 673–678.
34 S. P. Lee, M. L. Cunningham, P. C. Hines, C. C. Joneckis, E. P. Orringer and L. V. Parise, *Blood*, 1998, **92**, 2951–2958.
35 C. A. Hillery, M. C. Du, R. R. Montgomery and J. P. Scott, *Blood*, 1996, **87**, 4879–4886.
36 M. Udani, Q. Zen, M. Cottman, N. Leonard, S. Jefferson, C. Daymont, G. Truskey and M. J. Telen, *J. Clin. Invest.*, 1998, **101**, 2550–2558.
37 Q. Zen, M. Cottman, G. Truskey, R. Fraser and M. J. Telen, *J. Biol. Chem.*, 1999, **274**, 728–734.
38 P. C. Hines, Q. Zen, S. N. Burney, D. A. Shea, K. I. Ataga, E. P. Orringer, M. J. Telen and L. V. Parise, *Blood*, 2003, **101**, 3281–3287.
39 M. M. Murphy, M. A. Zayed, A. Evans, C. E. Parker, K. I. Ataga, M. J. Telen and L. V. Parise, *Blood*, 2005, **105**, 3322–3329.
40 P. P. Klug, N. Kaye and W. N. Jensen, *Blood Cells*, 1982, **8**, 175–184.
41 D. K. Kaul, M. E. Fabry and R. L. Nagel, *Proc. Natl. Acad. Sci. U. S. A.*, 1989, **86**, 3356–3360.
42 R. Zennadi, B. J. Moeller, E. J. Whalen, M. Batchvarova, K. Xu, S. Shan, M. Delahunty, M. W. Dewhirst and M. J. Telen, *Blood*, 2007, **110**, 2708–2717.
43 H. H. Lipowsky, *Microcirculation*, 2005, **12**, 5–15.
44 O. Linderkamp, E. Friederichs, T. Boehler and A. Ludwig, *Br. J. Haematol.*, 1993, **83**, 125–129.
45 Y. Alapan, C. Kim, A. Adhikari, K. E. Gray, E. Gurkan-Cavusoglu, J. A. Little and U. A. Gurkan, *Transl. Res.*, 2016, **173**(74-91), e78.
46 Y. Alapan, Y. Matsuyama, J. A. Little and U. A. Gurkan, *Technology*, 2016, **4**, 71–79.
47 G. A. Barabino, M. O. Platt and D. K. Kaul, *Annu. Rev. Biomed. Eng.*, 2010, **12**, 345–367.
48 M. Kim, Y. Alapan, A. Adhikari, J. A. Little and U. A. Gurkan, *Microcirculation*, 2017, **24**, e12374.
49 A. G. Koutsiaris, S. V. Tachmitzi, N. Batis, M. G. Kotoula, C. H. Karabatsas, E. Tsironi and D. Z. Chatzoulis, *Biorheology*, 2007, **44**, 375–386.
50 I. Okpala, *Blood Rev.*, 2004, **18**, 65–73.
51 C. C. Anyaegbu, I. E. Okpala, Y. A. Akren'Ova and L. S. Salimonu, *Eur. J. Haematol.*, 1998, **60**, 267–268.
52 L. R. Lard, F. P. Mul, M. de Haas, D. Roos and A. J. Duits, *J. Leukocyte Biol.*, 1999, **66**, 411–415.
53 A. J. Duits, J. B. Schnog, L. R. Lard, A. W. Saleh and R. A. Rojer, *Eur. J. Haematol.*, 1998, **61**, 302–305.
54 C. Mold, J. D. Tamerius and G. Phillips, Jr., *Clin. Immunol. Immunopathol.*, 1995, **76**, 314–320.
55 R. H. Wang, G. Phillips, Jr., M. E. Medof and C. Mold, *J. Clin. Invest.*, 1993, **92**, 1326–1335.
56 A. Kumar, J. R. Eckmam, R. A. Swerlick and T. M. Wick, *Blood*, 1996, **88**, 4348–4358.
57 P. Harmatz, E. Butensky, K. Quirolo, R. Williams, L. Ferrell, T. Moyer, D. Golden, L. Neumayr and E. Vichinsky, *Blood*, 2000, **96**, 76–79.
58 R. Raghupathy, D. Manwani and J. A. Little, *Adv. Hematol.*, 2010, **2010**, 272940.
59 A. Brownell, S. Lowson and M. Brozovic, *J. Clin. Pathol.*, 1986, **39**, 253–255.
60 J. Porter and M. Garbowski, *ASH Education Program Book*, 2013, **2013**, 447–456.
61 A. A. Akinbami, A. O. Dosunmu, A. A. Adediran, O. O. Oshinaike, V. O. Osunkalu, S. O. Ajibola and O. M. Arogundade, *J. Blood Med.*, 2013, **4**, 59–63.
62 E. Drasar, N. Vasavda, N. Igbineweka, M. Awogbade, M. Allman and S. L. Thein, *Br. J. Haematol.*, 2012, **157**, 645–647.
63 M. A. Sani, J. O. Adewuyi, A. S. Babatunde, H. O. Olawumi and R. O. Shittu, *Adv. Hematol.*, 2015, **2015**, 386451.
64 W. H. Wehrmacher and H. Messmore, *Postgraduate Haematology*, Oxford University Press, New York, 2000.
65 R. P. Hebbel, M. A. B. Boogaerts, J. W. Eaton and M. H. Steinberg, *N. Engl. J. Med.*, 1980, **302**, 992–995.
66 R. P. Hebbel, O. Yamada, C. F. Moldow, H. S. Jacob, J. G. White and J. W. Eaton, *J. Clin. Invest.*, 1980, **65**, 154–160.
67 N. Mohandas and E. Evans, *Blood*, 1984, **64**, 282–287.
68 R. P. Hebbel, *N. Engl. J. Med.*, 2000, **342**, 1910–1912.
69 R. H. Jensen, M. Vanderlaan, R. J. Grabske, E. W. Branscomb, W. L. Bigbee and L. H. Stanker, *Hemoglobin*, 1985, **9**, 349–362.
70 C. T. Quinn, M. C. Paniagua, R. K. DiNello, A. Panchal and M. Geisberg, *Br. J. Haematol.*, 2016, **175**, 724–732.
71 P. A. Smolinski, M. K. Offermann, J. R. Eckman and T. M. Wick, *Blood*, 1995, **85**, 2945–2950.
72 K. Sugihara and R. P. Hebbel, *Clin. Hemorheol.*, 1992, **12**, 185–189.
73 S. Taylor, S. Shacks and Z. Qu, *Immunol. Invest.*, 2001, **30**, 209–219.

74 K. Sugihara, T. Sugihara, N. Mohandas and R. P. Hebbel, *Blood*, 1992, **80**, 2634–2642.
75 R. A. Swerlick, J. R. Eckman, A. Kumar, M. Jeitler and T. M. Wick, *Blood*, 1993, **82**, 1891–1899.
76 T. M. Wick, J. L. Moake, M. M. Udden, S. G. Eskin, D. A. Sears and L. V. McIntire, *J. Clin. Invest.*, 1987, **80**, 905–910.
77 P. O. Olatunji and S. C. Davies, *Afr. J. Med. Med. Sci.*, 2000, **29**, 27–30.
78 I. Okpala, *Curr. Opin. Hematol.*, 2006, **13**, 40–44.
79 J. D. Belcher, C. Chen, J. Nguyen, L. Milbauer, F. Abdulla, A. I. Alayash, A. Smith, K. A. Nath, R. P. Hebbel and G. M. Vercellotti, *Blood*, 2014, **123**, 377–390.
80 F. A. Wagener, E. Feldman, T. de Witte and N. G. Abraham, *Proc. Soc. Exp. Biol. Med.*, 1997, **216**, 456–463.
81 G. Chen, D. Zhang, T. A. Fuchs, D. Manwani, D. D. Wagner and P. S. Frenette, *Blood*, 2014, **123**, 3818–3827.

